Magnetic structures of $R_2Fe_2Si_2C$ intermetallic compounds: Evolution to $Er_2Fe_2Si_2C$ and $Tm_2Fe_2Si_2C$

R. A. Susilo,[1,*] X. Rocquefelte,[2,†] J. M. Cadogan,[1] E. Bruyer,[2] W. Lafargue-Dit-Hauret,[2,3] W. D. Hutchison,[1] M. Avdeev,[4,5] D. H. Ryan,[6] T. Namiki,[7] and S. J. Campbell[1]

[1]*School of Science, UNSW Canberra at the Australian Defence Force Academy, Canberra BC 2610, Australia*
[2]*Université de Rennes, ENSCR, CNRS, ISCR (Institut des Sciences Chimiques de Rennes) - UMR 6226, F-35000 Rennes, France*
[3]*Physique Théorique des Matériaux, CESAM, Université de Liège, B-4000 Sart Tilman, Belgium*
[4]*Australian Centre for Neutron Scattering, Australian Nuclear Science and Technology Organisation, Lucas Heights, New South Wales 2234, Australia*
[5]*School of Chemistry, The University of Sydney, Sydney, New South Wales 2006, Australia*
[6]*Department of Physics, McGill University, Montreal, Québec H3A 2T8, Canada*
[7]*Graduate School of Science and Engineering, University of Toyama, Gofuku, Toyama 930-8555, Japan*

(Received 8 March 2019; revised manuscript received 11 April 2019; published 20 May 2019)

The magnetic structures of $Er_2Fe_2Si_2C$ and $Tm_2Fe_2Si_2C$ (monoclinic $Dy_2Fe_2Si_2C$-type structure, $C2/m$ space group) have been studied by neutron powder diffraction, complemented by magnetization, specific heat measurements, and ^{166}Er Mössbauer spectroscopy, over the temperature range 0.5 to 300 K. Their magnetic structures are compared with those of other $R_2Fe_2Si_2C$ compounds. Antiferromagnetic ordering of the rare-earth sublattice is observed below the Néel temperatures of $T_N = 4.8(2)$ K and $T_N = 2.6(3)$ K for $Er_2Fe_2Si_2C$ and $Tm_2Fe_2Si_2C$, respectively. While $Er_2Fe_2Si_2C$ and $Tm_2Fe_2Si_2C$ have the same crystal structure, they possess different magnetic structures compared with the other $R_2Fe_2Si_2C$ (R = Nd, Gd, Tb, Dy, and Ho) compounds. In particular, two different propagation vectors are observed below the Néel temperatures: $\mathbf{k} = [\frac{1}{2}, \frac{1}{2}, 0]$ (for $Er_2Fe_2Si_2C$) and $\mathbf{k} = [0.403(1), \frac{1}{2}, 0]$ (for $Tm_2Fe_2Si_2C$). For both compounds, the difference in propagation vectors is also accompanied by different orientations of the Er and Tm magnetic moments. Although the magnetic structures of $Er_2Fe_2Si_2C$ and $Tm_2Fe_2Si_2C$ differ from those of the other $R_2Fe_2Si_2C$ compounds, we have established that the two magnetic structures are closely related to each other. Our experimental and first-principles studies indicate that the evolution of the magnetic structures across the $R_2Fe_2Si_2C$ series is a consequence of the complex interplay between the indirect exchange interaction and crystal field effects.

DOI: 10.1103/PhysRevB.99.184426

I. INTRODUCTION

Rare-earth intermetallic compounds are known to exhibit a wide range of fascinating physical properties. Superconductivity, heavy-fermion behavior, Kondo effects, and charge density waves are several interesting properties found in this class of materials [1–5]. They also provide a unique platform for applications based on magnetocaloric effects (e.g., [6,7]). Most investigations on rare-earth intermetallics focus on their magnetic properties, which are known to show a strong dependence on the rare-earth ion. This stems from the fact that the magnetism of rare-earth intermetallic compounds is governed by the complex interplay between the indirect Ruderman-Kittel-Kasuya-Yosida (RKKY) exchange interaction and crystal field effects (CFE). As a result of these interactions, many rare-earth intermetallic compounds exhibit complex magnetic field-temperature phase diagrams [8], and a number of different magnetic structures have also been shown to exist across a series of rare-earth compounds [9].

Among various rare-earth based intermetallic compounds, those formed with rare-earth and transition metal elements (such as Fe, Co, and Ni) have attracted significant interest over the past three decades. Not only do they serve as the basis for permanent magnets, but these compounds allow us to study interactions between the localized $4f$ electrons of the rare-earth ions and the itinerant $3d$ electrons of the transition metal elements. Here, we will concentrate on one of the rare-earth transition metal compounds, $R_2Fe_2Si_2C$, in which the Fe atom was found to carry no magnetic moment [10–17].

The $R_2Fe_2Si_2C$ (R = Y, La–Nd, Sm, Gd–Tm) series of compounds was discovered by Paccard and Paccard [18] during their attempt to stabilize new compounds by adding small amounts of Si and C to the R-Fe binary system. These compounds crystallize in the monoclinic $Dy_2Fe_2Si_2C$-type structure with the $C2/m$ space group (no. 12). The R, Fe, and Si atoms occupy $4i$ sites (m point symmetry) in the unit cell with four atomic positions: $(x, 0, z)$, $(x + \frac{1}{2}, \frac{1}{2}, z)$, $(-x, 0, -z)$, and $(-x + \frac{1}{2}, \frac{1}{2}, -z)$, while the C atom occupies the $2a$ site ($2/m$ point symmetry) with two atomic positions: (0,0,0) and $(\frac{1}{2}, \frac{1}{2}, 0)$. The fractional coordinates of the R, Fe, and Si atoms do not vary significantly across the series and

*Present address: Center for High Pressure Science and Technology Advanced Research, Shanghai 201203, China; resta.susilo@hotmail.com
†xavier.rocquefelte@univ-rennes1.fr

are typically $x_R = 0.56$, $z_R = 0.29$, $x_{Fe} = 0.20$, $z_{Fe} = 0.10$, $x_{Si} = 0.15$, and $z_{Si} = 0.70$ [11,18].

The magnetic studies of the $R_2Fe_2Si_2C$ (R = Y, Pr, Nd, Gd, Tb, Dy, Ho, Er, and Tm) compounds by Schmitt *et al.* [10] and Pöttgen *et al.* [11] revealed that most of the compounds are antiferromagnetic, with Néel temperatures T_N ranging from $T_N \sim 45$ K for $Tb_2Fe_2Si_2C$ to $T_N \sim 2.4$ K for $Tm_2Fe_2Si_2C$. On the other hand no magnetic order was observed for $Y_2Fe_2Si_2C$, $Pr_2Fe_2Si_2C$, and $Lu_2Fe_2Si_2C$ down to 2 K [10,11,17]. Based on the magnetization measurements, the magnetism of the $R_2Fe_2Si_2C$ (R = Nd, Gd, Tb, Dy, Ho, Er, and Tm) compounds was attributed solely to the R atoms, i.e., the Fe atom was reported to be nonmagnetic. Subsequent neutron diffraction studies on $Nd_2Fe_2Si_2C$ and $Tb_2Fe_2Si_2C$ showed that the magnetic structures are characterized by the propagation vector of $\mathbf{k} = [0, 0, \frac{1}{2}]$ [19]. However, Le Roy *et al.* [19] arrived at a different conclusion regarding the magnetism of the Fe sublattice, in that they suggested that both the R and Fe sublattices are magnetically ordered at low temperature.

Recent neutron diffraction studies on $R_2Fe_2Si_2C$ (R = Gd, Tb, Dy, and Ho) [13–16] confirmed that the magnetic structures of these compounds are characterized by the propagation vector $\mathbf{k} = [0, 0, \frac{1}{2}]$ with the rare-earth magnetic moments pointing along the b axis. Spin-reorientation of the Dy magnetic moment is observed in $Dy_2Fe_2Si_2C$, in which the Dy magnetic moment rotates from the b axis towards the a-c plane on cooling below $T_t \sim 6$ K [16]. This spin-reorientation was shown to be driven by the competition between the second-order crystal field term and the higher-order terms [16]. ^{57}Fe Mössbauer spectroscopy measurements have been used to establish unambiguously that the Fe carries no magnetic moment in this series of compounds [13–17]. However, the magnetic structures of the remaining magnetic compounds in the series, $Er_2Fe_2Si_2C$ and $Tm_2Fe_2Si_2C$, have not been reported to date.

In order to fully understand the magnetic interactions in these compounds, it is of interest to follow the evolution of magnetic structures across this series. Although the magnetic structures of the $R_2Fe_2Si_2C$ (R = Gd–Ho) compounds determined previously are relatively simple, $Er_2Fe_2Si_2C$ and $Tm_2Fe_2Si_2C$ are expected to possess different magnetic structures due to the CFE. $Er_2Fe_2Si_2C$ and $Tm_2Fe_2Si_2C$ represent compounds where the R^{3+} ions possess a different sign of the second-order Stevens coefficients compared with the other $R_2Fe_2Si_2C$ (R = Tb, Dy, and Ho) compounds [20]. The change in sign of the second-order Stevens coefficients from negative (for R = Tb–Ho) to positive (for R = Er and Tm) is known to account for differences in the easy magnetization axis and orientations of the R magnetic moments across a series of rare-earth compounds (e.g., [21–24]).

In this paper, we have used neutron powder diffraction, complemented by magnetization, specific heat measurements and ^{166}Er Mössbauer spectroscopy, to determine the magnetic structures of $Er_2Fe_2Si_2C$ and $Tm_2Fe_2Si_2C$. We found that despite sharing similar crystal structure, the magnetic structures of $Er_2Fe_2Si_2C$ and $Tm_2Fe_2Si_2C$ are quite different from the other $R_2Fe_2Si_2C$ (R = Gd–Ho) compounds. Interestingly, although differing from the other $R_2Fe_2Si_2C$ compounds, the magnetic structures of $Er_2Fe_2Si_2C$ and $Tm_2Fe_2Si_2C$ are closely related to each other; this behavior is as expected given the same sign of the second-order Stevens coefficients for Er and Tm. In order to shed light on the observed magnetic behavior, we used first-principles calculations to calculate the stability of different magnetic structures in $Er_2Fe_2Si_2C$. A possible origin for the different magnetic structures in $Er_2Fe_2Si_2C$ and $Tm_2Fe_2Si_2C$ compared with other $R_2Fe_2Si_2C$ compounds will be discussed.

II. METHODS

A. Experiment

The polycrystalline samples of $R_2Fe_2Si_2C$ (R = Er and Tm) were prepared by arc-melting the high purity elements (at least 99.9 wt.%) under an argon atmosphere. The ingots were flipped and remelted several times to ensure homogeneity. X-ray powder diffraction (XRD) patterns were collected at room temperature using a PANalytical Empyrean diffractometer (Cu-$K\alpha$ radiation).

Magnetization and zero field specific heat data were measured using a Quantum Design Physical Property Measurement System (PPMS). Magnetization data were collected in the temperature range between 2 and 300 K in an applied field of $\mu_0 H = 0.5$ T (field-cooled mode). The specific heat measurements on $Er_2Fe_2Si_2C$ and $Tm_2Fe_2Si_2C$ were performed using a relaxation method between 2 and 300 K, while the specific heat of $Tm_2Fe_2Si_2C$ was measured between 0.5 and 300 K using a ^{3}He option. The ordering temperature was determined from the peak of the temperature derivatives of magnetization and the peak of the specific heat data.

Neutron diffraction experiments were carried out on the ECHIDNA high-resolution powder diffractometer [25] at the OPAL reactor (Sydney, Australia) with an incident neutron wavelength of 2.4395(5) Å. All diffraction patterns were corrected for absorption effects and were refined by the Rietveld method using the FULLPROF/WINPLOTR software [26,27].

The source for the ^{166}Er Mössbauer measurements was prepared by neutron irradiation of $Ho_{0.4}Y_{0.6}H_2$ to produce ~9 GBq of the ^{166}Ho parent isotope ($T_{1/2} = 26.9$ h). Both the source and sample were mounted vertically in a helium flow cryostat, and a high-purity germanium detector was used to isolate the 80.56 keV gamma rays. The spectrometer was operated in sine mode and calibrated using a laser interferometer. The spectrum was fitted using a full solution to the nuclear Hamiltonian [28].

B. Computation

Density functional theory (DFT) calculations were performed on the $Er_2Fe_2Si_2C$ compound. The calculations were carried out using the WIEN2K package [29], which is based on the augmented plane wave plus local orbitals (APW+lo) method. The plane-wave cutoff, defined by the product of the smallest atomic sphere radius times the magnitude of the largest reciprocal-lattice vectors (RMT_{min} and K_{max}), was set to 7.0 and a G_{max} (magnitude of the largest vector in the charge-density Fourier expansion) of 12 was used for all calculations. The muffin-tin radius are set to 2.50, 1.85, 1.84, and 1.44 a.u. for the Er, Fe, Si, and C atoms, respectively. Since it is well known that the generalized gradient approximation

(GGA) fails to predict the correct electronic ground states of systems with strongly correlated electrons, we have used the PBE0 hybrid on-site functional [30]. In this framework, 25% of the DFT exchange is replaced by Hartree-Fock exact exchange, leading to an improved description of the $4f$ states [30]. The lattice parameters and atomic positions derived from the experimental data were used in the calculation mainly for the following reasons: (i) The electric field gradient (EFG) is very sensitive to slight structural modifications. While the experimental accuracy on cell parameters is of the order of 0.0001 Å, it is about 0.1 Å in DFT, whatever functional is used. As a result, applying DFT optimized cell parameters usually leads to discrepancy in estimation of the EFG. (ii) The present system is based on both itinerant and localized electrons related to Fe($3d$) and Er($4f$) states, respectively. Such a system is very problematic to treat using one functional which could then lead to discrepancies in the optimized cell parameters.

III. RESULTS

A. Crystal structure

X-ray diffraction patterns collected at ambient conditions confirmed that both compounds crystallize in the monoclinic $Dy_2Fe_2Si_2C$-type structure ($C2/m$ space group). The refined lattice parameters are $a = 10.534(2)$ Å, $b = 3.8979(6)$ Å, $c = 6.6810(9)$ Å, $\beta = 129.08(1)^\circ$ for $Er_2Fe_2Si_2C$, and $a = 10.498(2)$ Å, $b = 3.885(1)$ Å, $c = 6.649(1)$ Å, $\beta = 128.99(1)^\circ$ for $Tm_2Fe_2Si_2C$. These values are in good agreement with previous reports [11,18].

B. Magnetization and specific heat

The magnetic susceptibilities of $Er_2Fe_2Si_2C$ and $Tm_2Fe_2Si_2C$ measured in an applied magnetic field of 0.5 T are shown in the left panel of Fig. 1. Cusp-like transitions associated with the antiferromagnetic transitions are clearly observable at $T_N = 4.8(2)$ K and $T_N = 2.6(2)$ K for $Er_2Fe_2Si_2C$ and $Tm_2Fe_2Si_2C$, respectively. The Curie-Weiss

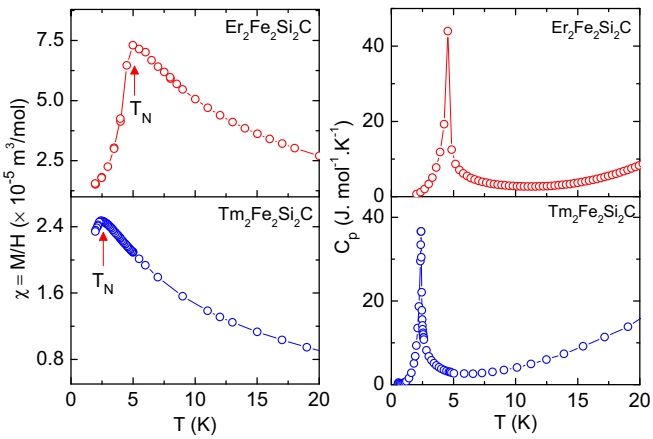

FIG. 1. (Left panel) The dc susceptibility of $Er_2Fe_2Si_2C$ and $Tm_2Fe_2Si_2C$ collected in field-cooled mode (FC; $\mu_0 H = 0.5$ T). The magnetic transition temperatures are marked by arrows. (Right panel) Zero field specific heat of $Er_2Fe_2Si_2C$ and $Tm_2Fe_2Si_2C$.

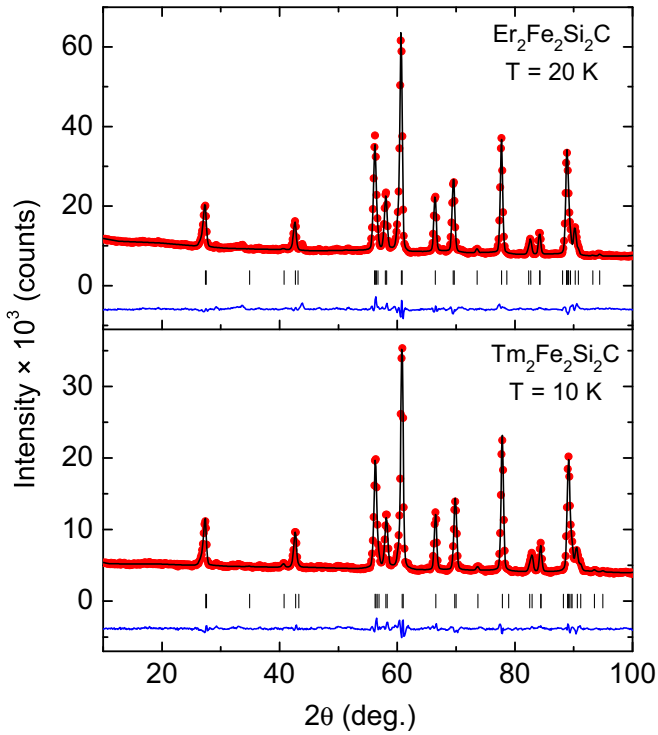

FIG. 2. Rietveld refinements of the neutron diffraction patterns of $Er_2Fe_2Si_2C$ and $Tm_2Fe_2Si_2C$ collected in the paramagnetic state. The vertical markers indicate Bragg reflections from the monoclinic $Dy_2Fe_2Si_2C$-type structure with the difference between the experimental and calculated patterns given by the blue line.

fits to the high temperature region of the inverse susceptibility data (not shown here) yield paramagnetic Curie temperatures of $\theta_P(\mathrm{Er}) = +5.9(6)$ K for $Er_2Fe_2Si_2C$ and $\theta_P(\mathrm{Er}) = +6(1)$ K for $Tm_2Fe_2Si_2C$. The effective moments, derived from the Curie-Weiss analyses, are $\mu_{\mathrm{eff}}(\mathrm{Er}) = 9.60(2)\mu_B$ and $\mu_{\mathrm{eff}}(\mathrm{Tm}) = 7.83(3)\mu_B$, close to the theoretical values of $9.58\mu_B$ and $7.56\mu_B$ for these R^{3+} ions. The specific heat data [$C_P(T)$], shown in the right panel of Fig. 1, also confirm the antiferromagnetic transitions occurring at $T_N \sim 4.8$ K (Er) and $T_N \sim 2.6$ K (Tm). These results agree with previous magnetic studies [10,11].

C. Neutron powder diffraction

Neutron diffraction patterns of $Er_2Fe_2Si_2C$ and $Tm_2Fe_2Si_2C$ collected in the paramagnetic state at 20 and 10 K, respectively, are presented in Fig. 2. Both diffraction patterns exhibit the nuclear scattering from the monoclinic $Dy_2Fe_2Si_2C$-type structure. The crystallographic data derived from the refinement of the 20 K (Er) and the 10 K (Tm) nuclear patterns are given in Table I.

The diffraction pattern of $Er_2Fe_2Si_2C$ obtained at 1.4 K, below the Néel temperature of $T_N \sim 4.8$ K (Fig. 3), shows considerable magnetic contributions from the Er sublattice, with the dominant magnetic peaks occurring at $2\theta \sim 20^\circ$, 32°, 38°, and 48°. It is clear that the magnetic structure of $Er_2Fe_2Si_2C$ is different from that of the $R_2Fe_2Si_2C$ compounds (R = Gd, Tb, Dy, and Ho) reported previously [13–16]. While the common magnetic structure of the

TABLE I. Crystallographic parameters of $Er_2Fe_2Si_2C$ and $Tm_2Fe_2Si_2C$ derived from the refinements of the neutron diffraction patterns obtained in the paramagnetic state (cf. Fig. 2).

	$Er_2Fe_2Si_2C$ $T = 20$ K	$Tm_2Fe_2Si_2C$ $T = 10$ K
x_R	0.5608(8)	0.5614(9)
z_R	0.294(1)	0.293(1)
x_{Fe}	0.2041(7)	0.2046(8)
z_{Fe}	0.099(1)	0.102(1)
x_{Si}	0.155(1)	0.153(1)
z_{Si}	0.705(2)	0.701(2)
a (Å)	10.5032(3)	10.4654(3)
b (Å)	3.8916(2)	3.8824(2)
c (Å)	6.6546(3)	6.6214(3)
β (°)	129.06(1)	128.96(1)
R_p (%); R_{wp} (%)	10.4; 8.8	12.2; 9.9
R_{Bragg} (%); R_F (%)	5.0; 4.0	5.1; 5.1

heavy-$R_2Fe_2Si_2C$ (R = Gd, Tb, Dy, and Ho) is characterized by an antiferromagnetic ordering of the R sublattice with $\mathbf{k} = [0, 0, \frac{1}{2}]$ [13–16], the additional magnetic peaks observed in the neutron diffraction pattern of $Er_2Fe_2Si_2C$ at 1.4 K can be indexed with a propagation vector of $\mathbf{k} = [\frac{1}{2}, \frac{1}{2}, 0]$, i.e., a cell-doubling along the a and b axes.

The possible magnetic structures allowed for the Er atom at the 4i site with $\mathbf{k} = [\frac{1}{2}, \frac{1}{2}, 0]$ were determined using the *BasIreps* program, part of the FULLPROF/WINPLOTR suite [26,27]. The decomposition of the magnetic representation comprises two components, each appearing three times:

$$\Gamma^{4i} = 3\Gamma_1 + 3\Gamma_2 \quad (1)$$

The basis vectors of these irreducible representations are given in Table II.

These two allowed magnetic structure models were tested, and the best refinement to the diffraction pattern at 1.4 K was obtained using the Γ_2 representation. While each irreducible representation allows the Er magnetic moment to point in any direction, initial attempts to refine all three components of the Er magnetic moment always yielded a small y component of the magnetic moment (close to zero within the uncertainty), i.e., $\mu_y^{Er} = 0.4(4)\mu_B$. A rather large uncertainty in the y component suggests that the Er magnetic moments lie in the a-c plane, thus in the final refinement the μ_y component was fixed at zero. We found that this approach did not affect the quality of the refinement as indicated by the identical values of the R factors. We therefore conclude that the Er magnetic moment is in the a-c plane at 1.4 K. The refined Er moment is $8.8(3)\mu_B$ (Table III), in agreement with the free-ion value of $9\mu_B$.

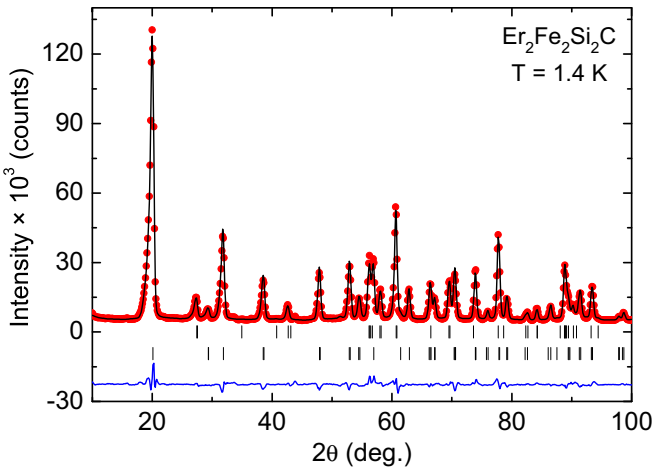

FIG. 3. Rietveld refinement of the neutron diffraction pattern of $Er_2Fe_2Si_2C$ collected at 1.4 K. The rows of Bragg markers, from top to bottom, represent $Er_2Fe_2Si_2C$ (nuclear) and $Er_2Fe_2Si_2C$ (magnetic), respectively. The difference between the experimental and calculated patterns is given by the blue line.

TABLE II. Representational analysis for the R atoms at the 4i site in $R_2Fe_2Si_2C$ with a propagation vector $\mathbf{k} = [\frac{1}{2}\ \frac{1}{2}\ 0]$. The columns for the atomic positions represent $R_1 = (x, 0, z)$, $R_2 = (x + \frac{1}{2}, \frac{1}{2}, z)$, $R_3 = (-x, 0, -z)$, and $R_4 = (x + \frac{1}{2}, \frac{1}{2}, -z)$.

	R_1	R_2	R_3	R_4
Γ_1	[u v w]	[u v w]	[u v w]	[u v w]
Γ_2	[u v w]	[u v w]	[−u − v − w]	[−u − v − w]

The diffraction pattern of $Tm_2Fe_2Si_2C$ obtained at 2.35 K, slightly below $T_N = 2.6(3)$ K (Fig. 4), shows the appearance of magnetic peaks due to the ordering of the Tm sublattice. These additional magnetic peaks cannot be indexed with either $\mathbf{k} = [0, 0, \frac{1}{2}]$, the common propagation vector for $R_2Fe_2Si_2C$ compounds (observed in R = Gd, Tb, Dy, and Ho [13–16]), or $\mathbf{k} = [\frac{1}{2}, \frac{1}{2}, 0]$, the propagation vector appropriate for $Er_2Fe_2Si_2C$. In addition, these magnetic contributions cannot be indexed using a simple multiplication of the crystallographic unit cell, which implies that the magnetic structure of $Tm_2Fe_2Si_2C$ is incommensurate with the nuclear unit cell. In order to determine the propagation vector, we used the *k_search* program, part of the FULLPROF suite [26], based on the peak positions of the observed magnetic satellites. A propagation vector of $\mathbf{k} = [k_x, \frac{1}{2}, 0]$ ($k_x \sim 0.401$) is able to index all magnetic reflections in the 2.35 K pattern. This propagation vector is close to the $\mathbf{k} = [\frac{1}{2}, \frac{1}{2}, 0]$ observed in $Er_2Fe_2Si_2C$. However the presence of an incommensurate x component of the propagation vector in $Tm_2Fe_2Si_2C$ indicates that the magnetic unit cell of $Tm_2Fe_2Si_2C$ along the a direction is larger than the magnetic unit cell in $Er_2Fe_2Si_2C$.

We again used the *BasIreps* program, in order to determine the possible magnetic structures allowed for the Tm atom at the 4i site with $\mathbf{k} = [k_x, \frac{1}{2}, 0]$ ($k_x \sim 0.401$). The decomposition of the magnetic representations are similar to the magnetic representation for $\mathbf{k} = [\frac{1}{2}, \frac{1}{2}, 0]$ in the case of $Er_2Fe_2Si_2C$, except that there is only a single irreducible representation in $Tm_2Fe_2Si_2C$, i.e., $\Gamma^{4i} = 3\Gamma_1$. Furthermore, in the presence of an incommensurate propagation vector, the Tm 4i site is split into two orbits, with the Tm magnetic moments related by the center of inversion no longer coupled to each other. Tm atoms at R_1 and R_2 form the first orbit whereas Tm atoms at R_3 and R_4 form the second orbit (see Table II). The appearance of two orbits suggests the possibility of having two magnetically inequivalent Tm sites

TABLE III. Crystallographic and magnetic parameters of $Er_2Fe_2Si_2C$ and $Tm_2Fe_2Si_2C$ derived from refinement of the neutron diffraction patterns obtained in the antiferromagnetic states (cf. Figs. 3, 4, and 6).

	$Er_2Fe_2Si_2C$	$Tm_2Fe_2Si_2C$	
	$T = 1.4$ K	$T = 2.35$ K	$T = 1.5$ K
x_R	0.5612(8)	0.561(1)	0.5604(8)
z_R	0.293(2)	0.293(3)	0.294(2)
x_{Fe}	0.204(1)	0.206(1)	0.205(1)
z_{Fe}	0.100(2)	0.098(3)	0.100(2)
x_{Si}	0.156(2)	0.156(3)	0.155(2)
z_{Si}	0.705(3)	0.709(4)	0.705(3)
a (Å)	10.5042(3)	10.458(1)	10.4663(6)
b (Å)	3.8923(2)	3.8792(4)	3.8831(2)
c (Å)	6.6557(3)	6.6185(6)	6.6229(4)
β (deg)	129.06(1)	129.06(1)	128.95(1)
propagation vector **k**	$[\frac{1}{2}, \frac{1}{2}, 0]$	[0.401(1), $\frac{1}{2}$, 0]	[0.403(2), $\frac{1}{2}$, 0]
commensurate			
μ_x^R (μ_B)	3.5(4)		
μ_y^R (μ_B)	0.0		
μ_z^R (μ_B)	10.6(2)		
μ_R (μ_B)	8.8(3)		
incommensurate			
$A_x(k)$ (μ_B)		2.1(6)	2.5(3)
$A_y(k)$ (μ_B)		0.0	0.0
$A_z(k)$ (μ_B)		7.0(3)	10.2(2)
$A(k)_{total}$ (μ_B)		5.9(4)	8.8(2)
$R_p(\%)$; $R_{wp}(\%)$	9.6; 10.2	14.0; 14.4	8.7; 9.3
$R_{Bragg}(\%)$; $R_F(\%)$	3.8; 2.6	3.3; 2.3	3.0; 1.7
$R_{mag}(\%)$	6.3	14.1	5.6 (1st), 10.9 (3rd), 15.5 (5th)

in $Tm_2Fe_2Si_2C$. It should also be noted that the absence of imaginary components of the basis vector allows us to rule out a helical magnetic structure of $Tm_2Fe_2Si_2C$.

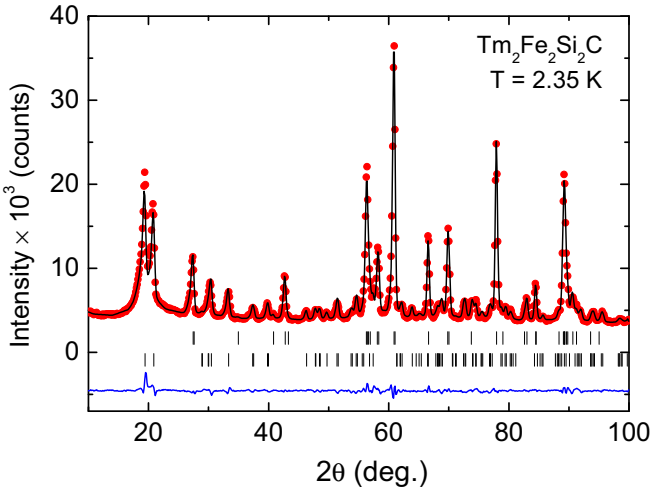

FIG. 4. Rietveld refinement of the neutron diffraction pattern of $Tm_2Fe_2Si_2C$ collected at 2.35 K. The rows of Bragg markers, from top to bottom, represent $Tm_2Fe_2Si_2C$ (nuclear) and $Tm_2Fe_2Si_2C$ (magnetic), respectively. The difference between the experimental and calculated patterns is given by the blue line.

Refinement of the $Tm_2Fe_2Si_2C$ pattern, collected at 2.35 K and using a sine-modulated magnetic structure along the a axis in which the magnetic moments of both orbits are constrained to be the same, yields a good fit to the data. Further refinements obtained on varying the phase difference between two orbits do not converge. In addition, convergence could not be achieved through varying the magnetic moment amplitudes of these two orbits independently. Similar to the case of $Er_2Fe_2Si_2C$, the refinement to the 2.35 K pattern by varying all the x, y, and z components of the Tm magnetic moment always led to a very small y component of the magnetic moment [$\mu_y^{Tm} = 0.2(2)\mu_B$]. The y component was fixed to zero in the final refinement. In Fig. 4, we show the refinement of the 2.35 K pattern using a sine-modulated magnetic structure with the wave running along the a axis and a cell-doubling along the b axis, with the Tm magnetic moments lying in the a-c plane. The refined amplitude $A(k)$ of the sine-modulated structure is $5.9(4)\mu_B$. The mean magnetic moment can be calculated using $\mu_{Tm} = A(k)/\sqrt{2}$, yielding a mean Tm magnetic moment of $4.2(3)\mu_B$ at 2.35 K. The refinement parameters for the 2.35 K neutron pattern are given in Table III.

Figure 5 contains plots of the low angle region of the neutron diffraction patterns of $Tm_2Fe_2Si_2C$ collected at various temperatures between 1.5 and 2.35 K. Several additional magnetic peaks are seen in the diffraction pattern collected below ~2 K, with the most prominent magnetic peaks occurring at $2\theta \sim 18°$, 23°, and 25°, suggesting a change in magnetic structure. These magnetic peaks can be indexed with

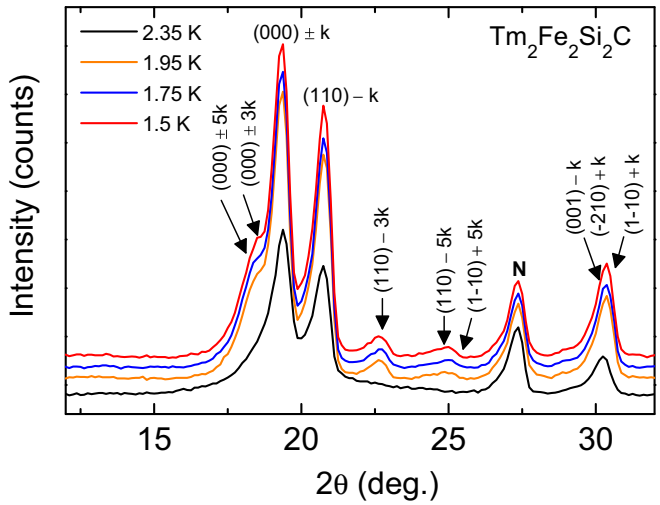

FIG. 5. Low angle region of neutron powder diffraction patterns of $Tm_2Fe_2Si_2C$ obtained at 2.35, 1.95, 1.75, and 1.5 K (bottom to top).

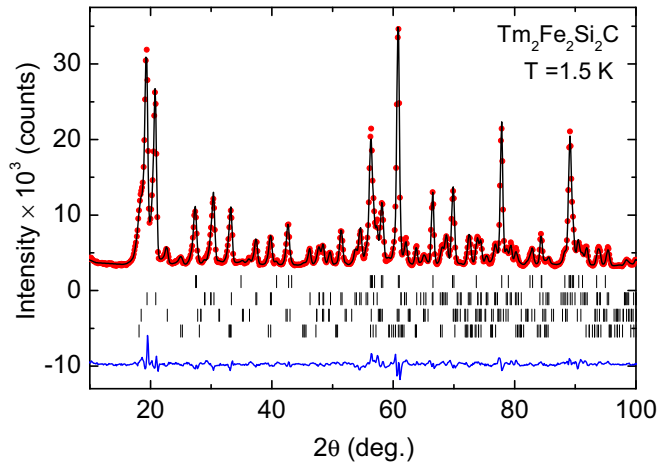

FIG. 6. Rietveld refinement of the neutron diffraction pattern of $Tm_2Fe_2Si_2C$ at 1.5 K. The rows of Bragg markers, from top to bottom, represent $Tm_2Fe_2Si_2C$ (nuclear) and $Tm_2Fe_2Si_2C$ magnetic (first, third, and fifth harmonics), respectively. The difference between the experimental and calculated patterns is given by the blue line.

two additional propagation vectors, $\mathbf{k}_2 = [0.209, \frac{1}{2}, 0]$ and $\mathbf{k}_3 = [0.015, \frac{1}{2}, 0]$, corresponding to the third- and fifth-order harmonics of the fundamental sine-wave, respectively. This indicates that the sine-modulated magnetic structure observed just below T_N transforms into a square-wave modulated magnetic structure on cooling below ∼2 K. This "squaring-up" transition is also observed in the case of thulium metal [31]. In general, a sine-modulated magnetic structure cannot be stabilized down to absolute zero due to entropy effects [32] and it will undergo either a transition into a square wave or lock in to a commensurate magnetic structure (see, e.g., Ref. [33]). In the case of $Tm_2Fe_2Si_2C$, we did not find any evidence of a lock-in transition to a commensurate structure. Rietveld refinement to the neutron pattern collected at 1.5 K is shown in Fig. 6.

The 1.5 K pattern of $Tm_2Fe_2Si_2C$ can be fitted well using a square-wave magnetic structure as discussed above. A similar approach as in the refinement to the 2.35 K pattern was used, in which the Tm magnetic moment is constrained to the *a*-*c* plane. We tried to include the *y* component of the magnetic moment, but the refined value of the *y* component is close to zero within the uncertainty. The refined amplitudes for the square wave are found to be $8.8(2)\mu_B$, $3.0(2)\mu_B$, and $1.8(2)\mu_B$ for the fundamental, third, and fifth harmonics, respectively. The Tm magnetic moment in a square-wave magnetic structure can be calculated from the amplitude $A(k)$ of the fundamental harmonic using $\mu_{\mathrm{Tm}} = A(k) \times \pi/4$ (e.g., Refs. [34,35]), yielding a refined Tm magnetic moment of $6.9(2)\mu_B$, in agreement with the free-ion value for Tm^{3+} ion ($gJ = 7.0$).

The magnetic structure of $Tm_2Fe_2Si_2C$ (hereafter labeled SQM) together with the magnetic structure of $Er_2Fe_2Si_2C$ (hereafter labeled AFM1) at 1.5 K projected onto the *a*-*c* plane are illustrated in Fig. 7. Despite the presence of an incommensurate *x* component of the propagation vector, this SQM structure has strong similarities with the AFM1 structure observed in $Er_2Fe_2Si_2C$ as is evident from Figs. 7(a) and 7(b). If we label a pair of magnetic moments with the "++" configuration as A, and a pair of magnetic moments with the "−−" configuration as B (+ and − represent magnetic moments pointing up and down, respectively), then the spin configuration along the *a* axis in the AFM1 structure is described by the sequence of BBAABBAABBAA [Fig. 7(a)]. The SQM structure itself can be described with the AB|AABBAABB|AB sequence along the *a* axis [Fig. 7(b)], which is derived from the AFM1 structure by introducing a spin discommensuration or spin-slip [36,37] block with an AB sequence in every fifth nuclear unit cell. Holmium metal is one well-known example where the spin-slip structure occurs [36,37]. This spin-slip block occurs and repeats almost every five nuclear unit cells, consequently the magnetic unit cell in the SQM structure is roughly five times larger than the nuclear unit cell along the *a* axis, as compared with the initial AFM1 structure where the magnetic unit cell is twice as large as the nuclear unit cell along the *a* direction.

D. ^{166}Er Mössbauer spectroscopy

^{166}Er Mössbauer spectroscopy has been used to complement the neutron diffraction experiments on $Er_2Fe_2Si_2C$. In Fig. 8, we show the ^{166}Er Mössbauer spectrum of $Er_2Fe_2Si_2C$ measured at 5 K. The spectrum is a well-resolved pentet expected for the $2 \rightarrow 0$ ^{166}Er transition, despite the fact that the spectrum was collected slightly above $T_N = 4.8(1)$ K. This result, together with a broader experimental linewidth at 5 K of 3.6(1) mm/s [as compared with the typical linewidth of 2.49(4) mm/s on the $ErFe_2$ calibration], reflects the likely impact of slow paramagnetic relaxation of the Er magnetic moments close to or just above the ordering temperature. The presence of slow Er^{3+} paramagnetic relaxation is commonly observed in Er-based compounds, and in some cases can persist well above the ordering temperature (e.g., Refs. [38–40]).

The spectrum at 5 K was fitted with a single pentet with an asymmetry parameter $\eta = 0$. The isomer shift is −0.07(7) mm/s, a negligible isomer shift as expected for

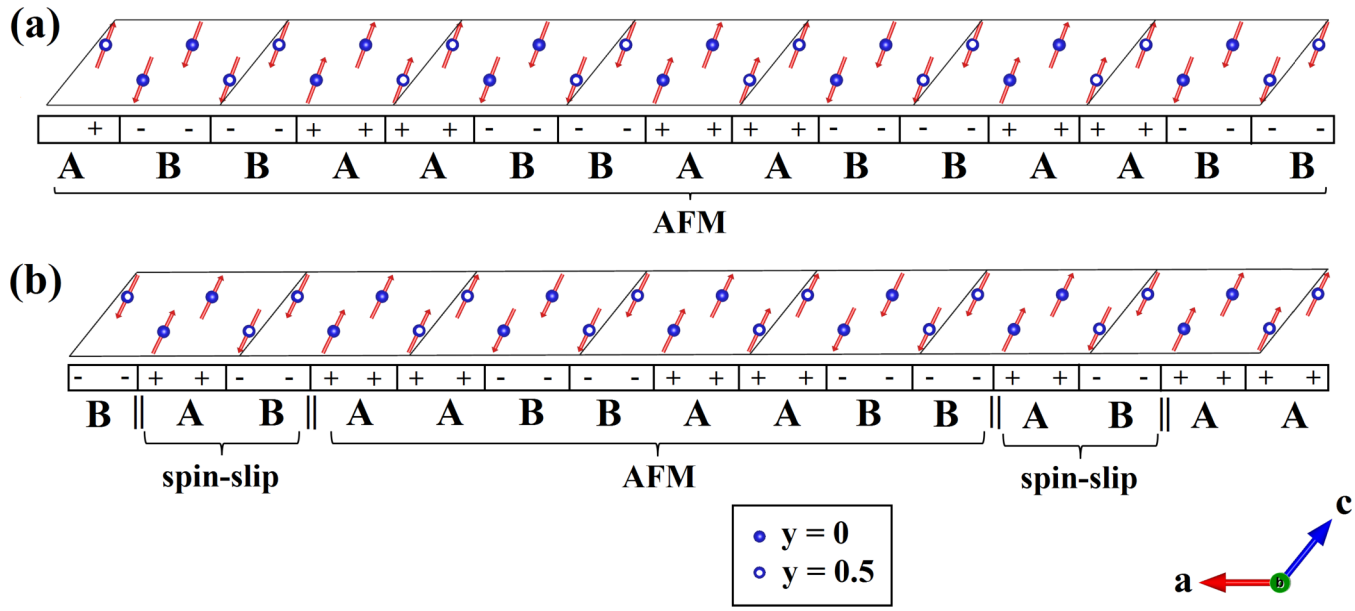

FIG. 7. Magnetic structures of (a) $Er_2Fe_2Si_2C$ and (b) $Tm_2Fe_2Si_2C$ at 1.5 K. The magnetic structure is projected onto the *a*-*c* plane to better illustrate the square-wave modulation of the Tm magnetic moment along the *a* axis. Each block corresponds to a nuclear unit cell. The Fe, Si, and C atoms are omitted for clarity.

a $2 \rightarrow 0$ rotational nuclear transition, while the quadrupole coupling constant eQV_{zz} is 16.0(3) mm/s, close to the free-ion value of 16.3(7) mm/s [41]. The fitted hyperfine field at the Er nucleus is 774(1) T. Using the moment to field conversion factor appropriate for the ^{166}Er nucleus of 87.2 ± 1.2 T/μ_B [38], this value converts to an Er magnetic moment of $8.8(2)\mu_B$ which implies a "fully stretched" $J = \frac{15}{2}$ ground state of the Er^{3+} ion. This result is in excellent agreement with the refined Er moment at 1.5 K of $8.8(3)\mu_B$ obtained from our neutron diffraction experiments.

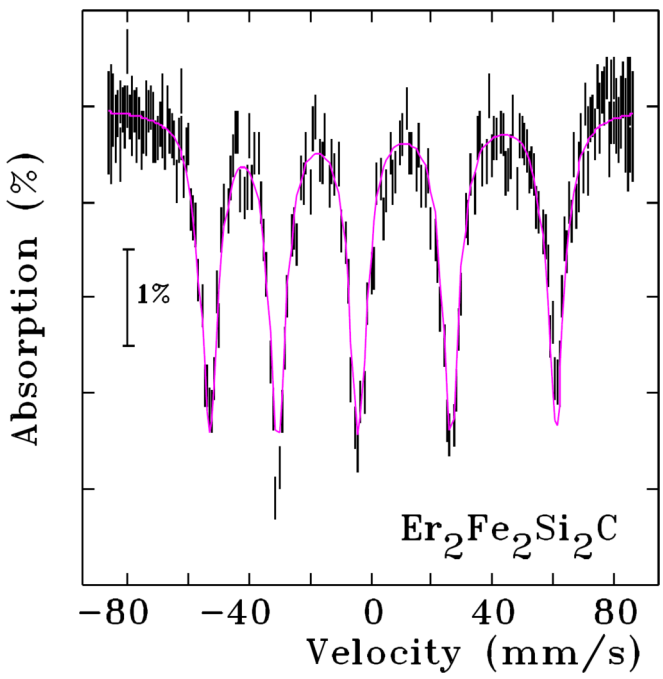

FIG. 8. ^{166}Er Mössbauer spectrum of $Er_2Fe_2Si_2C$ collected at 5 K.

E. Electronic structure calculations

An important finding from the neutron diffraction studies on the $R_2Fe_2Si_2C$ (R = Gd, Tb, Dy, Ho, Er, and Tm) compounds is the variation of magnetic structure across the series, which is particularly noticeable as we progress from R = Ho to R = Er. The compounds with R = Gd, Tb, Dy, and Ho order antiferromagnetically with $\mathbf{k} = [0, 0, \frac{1}{2}]$ (herein labeled AFM2) with the R magnetic moments pointing along the *b* axis [13–16]. For $Er_2Fe_2Si_2C$ the magnetic structure is characterized by $\mathbf{k} = [\frac{1}{2}, \frac{1}{2}, 0]$ (AFM1), while in $Tm_2Fe_2Si_2C$ the Tm magnetic moments form a sine-modulated magnetic structure just below T_N which squares up into a square-wave magnetic structure (SQM) below $T \sim 2$ K. In these latter two cases, the R magnetic moments lie in the *a*-*c* plane.

In order to understand the origin of this variation, we have calculated the relative stability of the two magnetic structures in the case of $Er_2Fe_2Si_2C$ using DFT simulations. Calculations were performed in a unit cell which accommodates AFM1 and AFM2 magnetic structures. These simulations were carried out taking into account the PBE0 on-site hybrid functional correction and spin-orbit coupling (PBE0+SO). The present PBE0+SO calculations also allow us to investigate the preferred R magnetic moment direction. Based on our calculations, we conclude that the AFM1 order is more stable than AFM2 by about 15 meV/f.u., which agrees well with the experimental results. The main results for the most stable magnetic order (AFM1) are summarized in Table IV. We found that the orientation of the Er magnetic moment is more energetically favorable along the *c* direction than the *a* and *b* directions, which are 16 and 28 meV/f.u. less stable, respectively. This result is also consistent with the findings determined from refinement of the neutron data, in which the Er magnetic moment lies in the *a*-*c* plane with the main component along the *c* direction.

TABLE IV. Energy differences (in meV per formula unit) for several magnetization directions of $Er_2Fe_2Si_2C$ in the AFM1 state. Calculations were done using the hybrid PBE0 on-site approach. For clarity, the energy differences are given with respect to that obtained for spins aligned along the [001] direction. The quadrupole coupling constant (eQV_{zz}) and the spin and orbital components (μ_{spin} and μ_{orb}, respectively) of the Er atom are also reported for each magnetization direction.

		[100]	[010]	[001]
ΔE (meV/f.u.)		16	28	0
$\lvert\mu_{spin}\rvert$ (μ_B)		2.97	2.97	2.97
$\lvert\mu_{orb}\rvert$ (μ_B)		5.58	5.93	5.93
$\lvert\mu_{tot}\rvert$ (μ_B)		8.55	8.90	8.90
eQV_{zz} (mm/s)	$Q = -2.7$ b [42,43]	14.0	16.4	13.1
	$Q = -2.9$ b [43,44]	15.1	17.7	14.0

The magnetic moment derived for Er of $8.90\mu_B$ is in good agreement with the refined value from neutron diffraction experiments. The calculated spin component μ_{spin} and orbital component μ_{orb} of the Er magnetic moment are $2.97\mu_B$ and 5.93 μ_B, respectively. The derived Fe magnetic moment is tiny (i.e., $\mu_{Fe} = 0.015\mu_B$), showing evidence of a nonmagnetic state for Fe atoms, in agreement with the experimental expectation. The total and projected densities of states (pDOS), calculated within the PBE0+SO for the AFM1 state of $Er_2Fe_2Si_2C$ are shown in Fig. 9. The ground state is found to be metallic, as expected. The $4f$ states of Er, represented in blue in Fig. 9(a), are far from the Fermi energy (E_F). After integrating the pDOS, we obtain 6.95 electrons and 3.98 electrons in the up and down channels, respectively. This outcome corresponds to 10.9 electrons in the $4f$ states, thus confirming the 3+ oxidation state of the Er atom in this intermetallic compound. pDOS of the other elements (Fe, Si, and C) are shown in Fig. 9(b). The density of states at E_F is dominated by the Fe($3d$), orbitals which indicates that the metallic nature of this compound is due to the itinerant electrons of Fe. It can be seen that for the Fe, C, and Si, the up and down spin channels of pDOS are almost symmetric, which implies a negligible or zero magnetic moment for each of these atoms. In the case of Fe, a weak polarization from the surrounding Er^{3+} magnetic moment exists, which leads to a small polarized magnetic moment at the Fe site. This result is also consistent with the observation of line broadening in the ^{57}Fe Mössbauer spectra measured below the antiferromagnetic ordering temperatures, attributed to a small transferred magnetic hyperfine field from the surrounding rare-earth magnetic moments [13–16]. By comparison, the Er-Er exchange interactions do not polarize the Si and C sites, which remain purely nonmagnetic.

In order to check the validity of our calculations, we have estimated the electric field gradient (EFG) and the resulting quadrupole coupling constant eQV_{zz} for the three magnetization directions. Two different electric quadrupole moment Q values have been reported for the ^{166}Er nucleus [42–44], and are considered in our analysis. The results are presented in Table IV with the derived eQV_{zz} values found to range from 13 to 18 mm/s. These values are consistent with the experimental value of 16 mm/s, deduced from the ^{166}Er Mössbauer spectrum collected at 5 K, and confirm the validity of our PBE0+SO calculations. Moreover, the similarity between the calculated eQV_{zz} along the b direction and the experimentally determined eQV_{zz} suggests that the principal z axis of the electric field gradient is parallel to the crystal b axis, which corresponds to the twofold symmetry axis in the monoclinic $C/2m$ space group.

In Fig. 10 we present a visualization of the ^{166}Er EFG eigenaxes of $Er_2Fe_2Si_2C$, deduced from the PBE0+SO calculation for three magnetization directions. Using a strategy similar to that used in a previous study [45], we can determine the EFG main directions by considering the nonspherical contribution of the electronic density inside the Er sphere. Charge depletion (excess) in the i direction corresponds to a positive (negative) V_{ii} value, and then negative (positive) eQV_{ii} value (due to the negative sign of Q). For instance, with $Q = -2.9$ b, V_{xx}, V_{yy}, and V_{zz} values are respectively 6.4×10^{21},

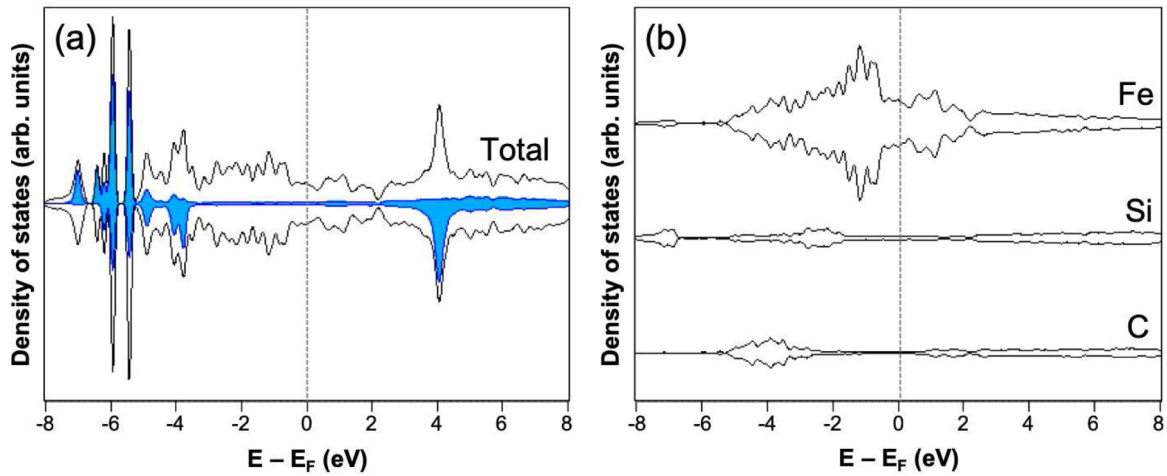

FIG. 9. Projected densities of states (pDOS) of the $Er_2Fe_2Si_2C$ compound based on the AFM1 order. The results were obtained using the PBE0+SO in WIEN2K, with magnetization along the [001] direction. The Fermi energy E_F has been defined as the reference energy and is represented by dashed lines. (a) Total DOS and partial DOS of one erbium site (in blue). (b) pDOS for three individual Fe, Si, and C sites. In all cases, majority and minority spin components are shown.

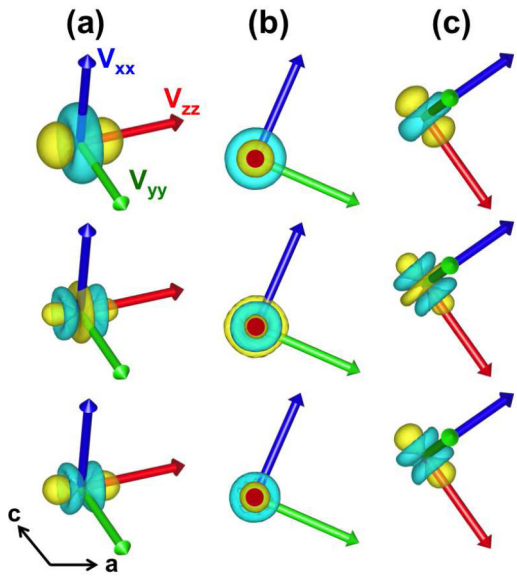

FIG. 10. Orientation of the ^{166}Er EFG eigenaxes of $Er_2Fe_2Si_2C$ based on AFM1 order and using the PBE0 functional and including SO with magnetization direction along (a) [100], (b) [010], and (c) [001]. Representations of the electronic densities inside the Er sphere report the contribution to the density when only the $|L| = 2$ (top), $|L| = 4$ (middle), and their sum (bottom) are considered. A light (dark) color is used for positive (negative) values.

6.6×10^{21}, and -13.0×10^{21} V m^{-2} when the magnetization is along the c direction. The corresponding eQV_{ii} values are -6.9, -7.1, and $+14.0$ mm/s for $i = x$, y, and z, respectively. Furthermore, it can be seen in Fig. 10(c) that for $Q = -2.9$ b, eQV_{zz} is positive and oriented along the positive part of the nonspherical density. By comparison, eQV_{xx} and eQV_{yy}, which are negative, are directed along the negative part of the charge density.

IV. DISCUSSION

The magnetic structures of the $R_2Fe_2Si_2C$ (R = Gd–Tm) compounds determined from neutron diffraction experiments are summarized in Table V. The compounds with R = Gd–Ho order antiferromagnetically with $\mathbf{k} = [0, 0, \frac{1}{2}]$ and with the R magnetic moments pointing along the b axis. For $Er_2Fe_2Si_2C$, the magnetic structure is characterized by $\mathbf{k} = [\frac{1}{2}, \frac{1}{2}, 0]$. In $Tm_2Fe_2Si_2C$, the Tm magnetic moments form a sine-modulated magnetic structure just below T_N, which transforms to a square-wave magnetic structure below $T \sim 2$ K. In these latter two cases, the R magnetic moments are in the a-c plane.

In a series of compounds where the R^{3+} ion is the only ion bearing a magnetic moment, the observed magnetic ordering of the system is a result of the indirect exchange interaction (RKKY) and the influence of CFE. Therefore, such a variation in magnetic structures for the $R_2Fe_2Si_2C$ series, particularly as the rare-earth ion changes from Ho^{3+} to Er^{3+}, is mostly related to two mechanisms. First, as we move towards the end of the R series, the R-R interatomic distances decrease (i.e., the lanthanide contraction). Thus, changes in the R-R exchange interactions are possible if the exchange couplings in $Ho_2Fe_2Si_2C$ are close to zero points of the oscillatory RKKY function. The second mechanism is the effect of the crystal field acting on the R^{3+} ion, since the Ho^{3+} and Er^{3+} ions have opposite signs of the second-order Stevens coefficient.

Since $Ho_2Fe_2Si_2C$ and $Er_2Fe_2Si_2C$ have similar interatomic distances between the R^{3+} ions, we suggest that the evolution of the magnetic structures across this series of compounds is not the result of the RKKY exchange interaction alone. Moreover, given that the change in the magnetic propagation vector from $\mathbf{k} = [0, 0, \frac{1}{2}]$ ($R^{3+} = Ho^{3+}$) to $\mathbf{k} = [\frac{1}{2}, \frac{1}{2}, 0]$ ($R^{3+} = Er^{3+}$) is also accompanied by a change in the direction of the R moment due to CFE, it is likely that there is an interplay between these two variables. Such a case has already been reported in the R_2CoGa_8 series of compounds [46–49]. Joshi *et al.* [46] determined the crystal-field dependence of the in-plane (J_{ex}^{ab}) and the out-of-plane (J_{ex}^{c}) exchange couplings of R_2CoGa_8 (R = Tb–Tm) from single-crystal susceptibility measurements. In addition to the opposite signs of the second-order B_2^0 parameter as one progresses from R = Ho to R = Er (which reflects the change in the magnetic anisotropy), they found that the relative strengths between the in-plane and out-of-plane exchange couplings (defined as $\Delta J_{ex} = J_{ex}^{c} - J_{ex}^{ab}$) change from negative (as observed in R = Tb–Ho) to positive for Er_2CoGa_8 and becomes increasingly positive for Tm_2CoGa_8. Consequently, the variation of the magnetic structures observed in the R_2CoGa_8 series of compounds from $\mathbf{k}_1 = [\frac{1}{2}, \frac{1}{2}, \frac{1}{2}]$ for R = Gd–Ho to $\mathbf{k}_2 = [0, \frac{1}{2}, 0]$ for R = Er and $\mathbf{k}_3 = [\frac{1}{2}, 0, \frac{1}{2}]$ for R = Tm was attributed to this sign reversal of ΔJ_{ex} due to CFE [48].

TABLE V. The magnetic structures of the $R_2Fe_2Si_2C$ (R = Gd–Tm) compounds derived from neutron diffraction experiments. **k** is the magnetic propagation vector and MMD represents the magnetic moment direction.

Compound	**k**	MMD	Reference
$Gd_2Fe_2Si_2C$	$[0, 0, \frac{1}{2}]$	b axis	[14]
$Tb_2Fe_2Si_2C$	$[0, 0, \frac{1}{2}]$	b axis	[15]
$Dy_2Fe_2Si_2C$	$[0, 0, \frac{1}{2}]$	b axis ($T > T_t$)	[16]
	$[0, 0, \frac{1}{2}]$	canted towards the a-c plane ($T < T_t$)	
$Ho_2Fe_2Si_2C$	$[0, 0, \frac{1}{2}]$	b axis	[13]
$Er_2Fe_2Si_2C$	$[\frac{1}{2}, \frac{1}{2}, 0]$	a-c plane	present work
$Tm_2Fe_2Si_2C$	$[0.403(1), \frac{1}{2}, 0]$	a-c plane	present work

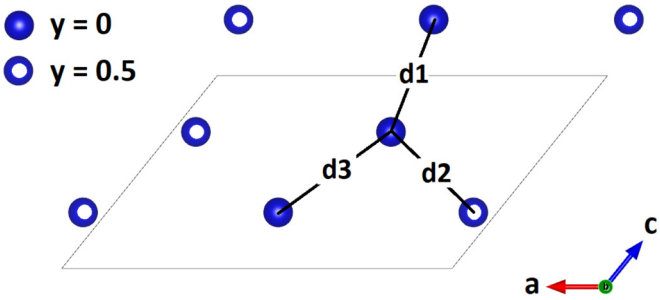

FIG. 11. Local arrangement of the Tm atoms in $Tm_2Fe_2Si_2C$ projected onto the *a*-*c* plane.

In order to understand why the SQM structure in $Tm_2Fe_2Si_2C$ can be stabilized in the first place, we examine the nearest-neighbor environment of the Tm atom in $Tm_2Fe_2Si_2C$ shown in Fig. 11. As indicated in Fig. 11, there are three shortest Tm-Tm separations (labeled by d_1, d_2, and d_3), each with a distance of less than 4 Å. In Fig. 12 we show the temperature dependence of these Tm-Tm separations as derived from the neutron diffraction refinements.

Below $T_N = 2.6(2)$ K, the d_1 separation undergoes a slight increase which might be associated with small magnetoelastic effects occurring below the ordering temperature as observed in $Tb_2Fe_2Si_2C$ [15]. An interesting feature, however, is seen with the d_2 and d_3 separations. In the paramagnetic state (at 10 K), the difference between the d_2 and d_3 separations in $Tm_2Fe_2Si_2C$ is ∼0.05 Å, while, on cooling below $T_N \sim 2.6$ K, the d_3 separation decreases whereas the d_2 separation increases. Below $T \sim 2$ K, where the squaring-up transition occurs, these two separations merge to approximately the same value of ∼3.66 Å. This feature is unique to $Tm_2Fe_2Si_2C$, and is not observed in other $R_2Fe_2Si_2C$ compounds (for comparison, the difference between the d_2 and d_3 separations in $Er_2Fe_2Si_2C$ is ∼0.05 Å at 1.5 K, below its Néel temperature of $T_N \sim 4.8$ K).

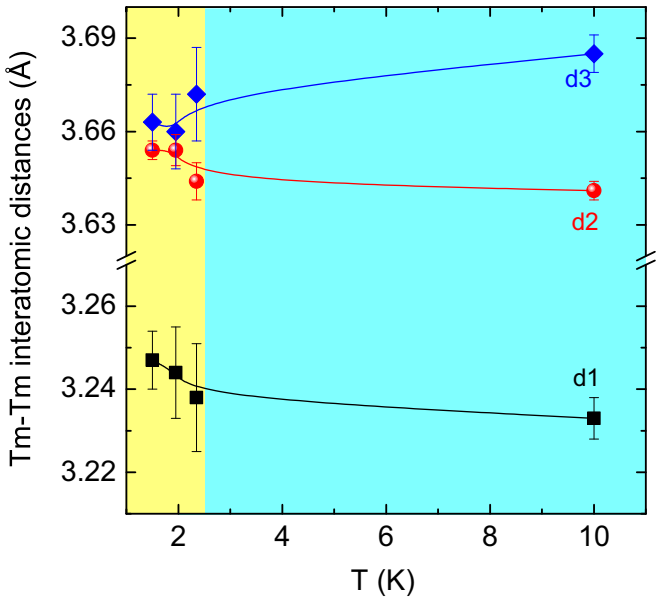

FIG. 12. Temperature dependences of the Tm-Tm interatomic distances d_1, d_2, and d_3 (Fig. 11) in $Tm_2Fe_2Si_2C$ ($T_N \sim 2.6$ K) as derived from the neutron diffraction refinements. Solid lines are guides to the eyes.

It is known that the strength of the indirect RKKY exchange interaction in rare-earth (*R*) based intermetallic compounds is strongly related to the *R*-*R* interatomic distances. As outlined above, formation of the SQM structure in $Tm_2Fe_2Si_2C$ is also accompanied by the increasing and decreasing of the d_2 and d_3 separations, respectively, with the two having similar interatomic distance below $T \sim 2$ K. These results suggest that the SQM structure can be stabilized by the change in the relative strength of the nearest-neighbor exchange couplings associated with these two separations (i.e., j_2 and j_3). The similar distances of the d_2 and d_3 separations could therefore lead to a competing interaction between j_2 and j_3 (since $|j_2| \approx |j_3|$ in such a case). Such competition can lead to magnetic frustration along the *a* axis, which in turn may stabilize the SQM structure in $Tm_2Fe_2Si_2C$. We note that although this model can be used to explain why the SQM structure is allowed, the fundamental reason as to why the SQM structure is preferred over the AFM2 structure in $Tm_2Fe_2Si_2C$ remains unclear.

Based on the magnetic structures observed in $R_2Fe_2Si_2C$ (R = Gd, Tb, Ho, Er, and Tm) presented in Table V, it is evident that the evolution of the magnetic structures in this series of compounds is due to the competition between the exchange interaction and the CFE. To this end, we propose a possible mechanism responsible for the variation of the magnetic structures in the $R_2Fe_2Si_2C$ series which involves the interplay between the exchange interaction and the influence of the CFE as an attempt to minimize the overall magnetic energy of the system. In particular, we suggest that when the CFE force the *R* moment to align along the *b* axis, the system favors the AFM2 structure, whereas when the CFE force the *R* moment to order in the *a*-*c* plane, the AFM1 structure is preferred. This is also supported by our first-principles calculations which show that in $Er_2Fe_2Si_2C$, the AFM1 structure with the Er magnetic moment pointing along the *c* axis is a more stable magnetic configuration than the AFM2 structure. We also found that the SQM structure observed in $Tm_2Fe_2Si_2C$ can be derived from the AFM1 structure (observed in $Er_2Fe_2Si_2C$) by introducing a spin-slip block in every five nuclear unit cells (Fig. 7). Therefore, the above scenario is also valid in the case of $Tm_2Fe_2Si_2C$. In order to establish this mechanism, it would be of interest to investigate the effects of chemical pressure on the magnetic structure of $Ho_2Fe_2Si_2C$, i.e., by partial substitution of Ho with a smaller rare-earth ion such as Lu. If the RKKY exchange interaction is a more dominant factor in determining the magnetic structures in the $R_2Fe_2Si_2C$ compounds, we would expect that the magnetic structure of $Ho_2Fe_2Si_2C$ would transform from $\mathbf{k} = [0, 0, \frac{1}{2}]$ to $\mathbf{k} = [\frac{1}{2}, \frac{1}{2}, 0]$ at a certain Lu concentration. This aspect of study is currently under way.

V. CONCLUSIONS

We have determined the magnetic structures of $Er_2Fe_2Si_2C$ and $Tm_2Fe_2Si_2C$ below the antiferromagnetic transitions. The magnetic structure of $Er_2Fe_2Si_2C$ below $T_N = 4.8(2)$ K is commensurate antiferromagnetic in the *a*-*c* plane with

a propagation vector of $\mathbf{k} = [\frac{1}{2}, \frac{1}{2}, 0]$, whereas a sine-modulated magnetic structure is observed in $Tm_2Fe_2Si_2C$ ($\mathbf{k} = [0.403(1), \frac{1}{2}, 0]$) just below $T_N = 2.6(3)$ K. On cooling below ∼2 K, this sine-modulated magnetic structure of $Tm_2Fe_2Si_2C$ squares up into a square-modulated magnetic structure with the Tm magnetic moments lying in the *a*-*c* plane. Our DFT calculations reveal that the magnetic structure with a propagation vector of $\mathbf{k} = [\frac{1}{2}, \frac{1}{2}, 0]$, and the magnetic moment in the *a*-*c* plane is more energetically favorable in $Er_2Fe_2Si_2C$ than antiferromagnetic order with $\mathbf{k} = [0, 0, \frac{1}{2}]$ and *b*-axis order. The different magnetic structures observed in these compounds compared with other $R_2Fe_2Si_2C$ compounds (R = Gd, Tb, Dy, and Ho) are mostly a consequence of the complex interplay between the indirect exchange interaction and crystal field effects occurring in the $R_2Fe_2Si_2C$ series of compounds.

ACKNOWLEDGMENTS

R.A.S. acknowledges support via a Research Publication Fellowship from UNSW Canberra. The source activations were carried out by M. Butler at the McMaster Nuclear Reactor (Hamilton, Ontario). The theoretical work was granted access to the HPC resources of [TGCC/CINES/IDRIS] under the allocation 2017-A0010907682 made by GENCI. Financial support for various stages of this work was provided by the Natural Sciences and Engineering Research Council of Canada and Fonds pour la formation de chercheurs et l'aide á la recherche, Québec.

[1] R. J. Cava, H. Takagi, H. W. Zandbergen, J. J. Krajewski, W. F. Peck Jr., T. Siegrist, B. Batlogg, R. B. van Dover, R. J. Felder, K. Mizuhashi, J. O. Lee, H. Eisaki, and S. Uchida, Nature (London) **367**, 252 (1994).

[2] E. DiMasi, M. C. Aronson, J. F. Mansfield, B. Foran, and S. Lee, Phys. Rev. B **52**, 14516 (1995).

[3] R. Movshovich, M. Jaime, J. D. Thompson, C. Petrovic, Z. Fisk, P. G. Pagliuso, and J. L. Sarrao, Phys. Rev. Lett. **86**, 5152 (2001).

[4] M. F. Hundley, J. L. Sarrao, J. D. Thompson, R. Movshovich, M. Jaime, C. Petrovic, and Z. Fisk, Phys. Rev. B **65**, 024401 (2001).

[5] C. Malliakas, S. J. L. Billinge, H. J. Kim, and M. G. Kanatzidis, J. Am. Chem. Soc. **127**, 6510 (2005).

[6] V. K. Pecharsky and K. A. Gschneidner Jr., Phys. Rev. Lett. **78**, 4494 (1997).

[7] E. M. Levin, V. K. Pecharsky, and K. A. Gschneidner, Phys. Rev. B **60**, 7993 (1999).

[8] D. Gignoux and D. Schmitt, in *Handbook of Magnetic Materials*, edited by K. H. J. Buschow (Elsevier Science, North Holland, 1997), Vol. 10, Chap. 2, pp. 239–413.

[9] A. Szytula, in *Handbook of Magnetic Materials*, edited by K. H. J. Buschow (Elsevier Science, North Holland, 1991), Vol. 6, Chap. 2, pp. 85–180.

[10] D. Schmitt, D. Paccard, and L. Paccard, Solid State Commun. **84**, 357 (1992).

[11] R. Pöttgen, T. Ebel, C. B. H. Evers, and W. Jeitschko, J. Solid State Chem. **114**, 66 (1995).

[12] R. A. Susilo, J. M. Cadogan, W. D. Hutchison, and S. J. Campbell, Phys. Status Solidi A **211**, 1087 (2014).

[13] R. A. Susilo, J. M. Cadogan, R. Cobas, W. D. Hutchison, M. Avdeev, and S. J. Campbell, J. Appl. Phys. **117**, 17C113 (2015).

[14] D. H. Ryan, N. Mas, R. A. Susilo, J. M. Cadogan, and R. Flacau, J. Phys.: Condens. Matter **27**, 146005 (2015).

[15] R. A. Susilo, J. M. Cadogan, W. D. Hutchison, M. Avdeev, R. Cobas, S. Muñoz-Pérez, and S. J. Campbell, J. Alloys Compd. **654**, 392 (2016).

[16] R. A. Susilo, J. M. Cadogan, W. D. Hutchison, G. A. Stewart, M. Avdeev, and S. J. Campbell, J. Phys.: Condens. Matter **29**, 115806 (2017).

[17] R. A. Susilo, C.-H. Hsu, H. Lin, J. M. Cadogan, W. D. Hutchison, and S. J. Campbell, J. Alloys Compd. **778**, 618 (2019).

[18] L. Paccard and D. Paccard, J. Less Common Met. **136**, 297 (1988).

[19] J. Le Roy, D. Paccard, C. Bertrand, J. L. Soubeyroux, J. Bouillot, L. Paccard, and D. Schmitt, Solid State Commun. **86**, 675 (1993).

[20] K. W. H. Stevens, Proc. Phys. Soc. A **65**, 209 (1952).

[21] G. Venturini, P. Lemoine, B. Malaman, and B. Ouladdiaf, J. Alloys Compd. **505**, 404 (2010).

[22] E. D. Mun, S. L. Bud'ko, H. Kob, G. J. Miller, and P. C. Canfield, J. Magn. Magn. Mater. **322**, 3527 (2010).

[23] P. Lemoine, A. Verniére, G. Venturini, S. Capelli, and B. Malaman, J. Magn. Magn. Mater. **324**, 961 (2012).

[24] L. L. Zhao, M. S. Mehlman, T. Besara, T. Siegrist, and E. Morosan, J. Magn. Magn. Mater. **341**, 6 (2013).

[25] M. Avdeev and J. R. Hester, J. Appl. Crystallogr. **51**, 1597 (2018).

[26] J. Rodríguez-Carvajal, Physica B (Amsterdam) **192**, 55 (1993).

[27] T. Roisnel and J. Rodríguez-Carvajal, Mater. Sci. Forum **378–381**, 118 (2001).

[28] C. J. Voyer and D. H. Ryan, Hyperfine Interact. **170**, 91 (2006).

[29] P. Blaha, K. Schwarz, G. K. H. Madsen, D. Kvasnicka, J. Luitz, R. Laskowski, F. Tran, and L. D. Marks, *WIEN2k, An Augmented Plane Wave + Local Orbitals Program for Calculating Crystal Properties* (Technische Universität Wien, Vienna, 2018).

[30] F. Tran, P. Blaha, K. Schwarz, and P. Novák, Phys. Rev. B **74**, 155108 (2006).

[31] W. C. Koehler, J. W. Cable, E. O. Wollan, and M. K. Wilkinson, Phys. Rev. **126**, 1672 (1962).

[32] R. J. Elliott, Phys. Rev. **124**, 346 (1961).

[33] J. Rossat-Mignod, in *Neutron Scattering*, edited by K. Sköld and D. Price, Methods of Experimental Physics (Academic Press, Washington, 1987), Vol. 23C, Chap. 19, pp. 29–44.

[34] J. W. Lynn, S. Skanthakumar, Q. Huang, S. K. Sinha, Z. Hossain, L. C. Gupta, R. Nagarajan, and C. Godart, Phys. Rev. B **55**, 6584 (1997).

[35] M. Reehuis, G. Kotzyba, W. Jeitschko, and M. Hofmann, J. Magn. Magn. Mater. **221**, 307 (2000).

[36] R. A. Cowley and S. Bates, J. Phys. C **21**, 4113 (1988).

[37] J. Simpson, D. McMorrow, R. Cowley, and D. Jehan, J. Magn. Magn. Mater. **140–144**, 751 (1995).

[38] D. H. Ryan, J. M. Cadogan, and R. Gagnon, Phys. Rev. B **68**, 014413 (2003).
[39] D. H. Ryan, N. R. Lee-Hone, and G. A. Stewart, Solid State Phenom. **194**, 84 (2013).
[40] A. Legros, D. H. Ryan, P. Dalmas de Réotier, A. Yaouanc, and C. Marin, J. Appl. Phys. **117**, 17C701 (2015).
[41] B. Bleaney, in *Magnetic Properties of Rare Earth Metals*, edited by R. Elliot (Plenum, London, 1972), Chap. 8, pp. 29–44.
[42] Physics Division Annual Progress Report for Period Ending December 31, 1969, Oak Ridge National Laboratory Technical Report No. 4513, 1970 (unpublished).
[43] N. J. Stone, At. Data Nucl. Data Tables **90**, 75 (2005).
[44] G. Kaspar, W. Knupfer, W. Ebert, P. Holleczek, and N. Fiebiger, in *Proceedings of the International Conference on Nuclear Reactions Induced by Heavy Ions, Heidelberg, 1969*, edited by R. Bock and W. Hering (North-Holland Publishing Company, Amsterdam, 1970), p. 471.
[45] A. Sadoc, M. Body, C. Legein, M. Biswal, F. Fayon, X. Rocquefelte, and F. Boucher, Phys. Chem. Chem. Phys. **13**, 18539 (2011).
[46] D. A. Joshi, R. Nagalakshmi, S. K. Dhar, and A. Thamizhavel, Phys. Rev. B **77**, 174420 (2008).
[47] C. Adriano, C. Giles, L. Coelho, G. Faria, and P. Pagliuso, Physica B (Amsterdam) **404**, 3289 (2009).
[48] R. D. Johnson, T. Frawley, P. Manuel, D. D. Khalyavin, C. Adriano, C. Giles, P. G. Pagliuso, and P. D. Hatton, Phys. Rev. B **82**, 104407 (2010).
[49] J. R. L. Mardegan, C. Adriano, R. F. C. Vescovi, G. A. Faria, P. G. Pagliuso, and C. Giles, Phys. Rev. B **89**, 115103 (2014).